Journal of Alloys and Compounds 995 (2024) 174757

Contents lists available at ScienceDirect

Journal of Alloys and Compounds

journal homepage: www.elsevier.com/locate/jalcom

The $La_2Pd_3(Si, Ge)_5$ complete solid solution: Crystal structure, chemical bonding, and volume chemistry

Riccardo Freccero *, Pavlo Solokha, Serena De Negri

Università degli Studi di Genova, Dipartimento di Chimica e Chimica Industriale, Via Dodecaneso 31, Genova I-16146, Italy

ARTICLE INFO

Keywords:
Intermetallic compounds
Rare earths tetrelides
Quaternary alloys
Volume chemistry
Chemical bonding

ABSTRACT

The $La_2Pd_3Si_5$ intermetallic and the $La_2Pd_3(Si_xGe_{1-x})_5$ solid solution were targeted for structural and computational investigations. The ternary compound and quaternary alloys with varying silicon contents ($x = 0.25$, 0.50, 0.70, 0.75) were prepared by arc melting and turned out to crystalize with the *oI*40–$U_2Co_3Si_5$ (*Ibam*, N. 72) type structure based on powder X-ray diffraction data. The crystal structure of $La_2Pd_3Si_5$ was additionally solved through X-ray diffraction on single crystal grown by recrystallization in Sn flux. Chemical bonding investigations based on QTAIM effective charges and DOS/(I)COHP analysis indicate the formation of heteropolar interactions between Si and the surrounding La/Pd metals, and between La and Pd. Covalently bonded zigzag chains of Si are also formed and considered to be the main responsible for the higher melting point of $La_2Pd_3Si_5$, measured by DSC, with respect to that of $La_2Pd_3Ge_5$. The formation of a complete solid solution between $La_2Pd_3Si_5$ and $La_2Pd_3Ge_5$ was confirmed and refined unit cell parameters and volumes change linearly with composition, displaying a Vegard trend. The calculation of atomic volumes on a quantum chemical basis (QTAIM) provides detailed insights into the volume chemistry of $La_2Pd_3(Si_xGe_{1-x})_5$. Through this analysis La is found to be responsible, together with the gradual substitution of Ge with Si, for the volume contraction.

1. Introduction

Ternary $RE_2M_3X_5$ intermetallic compounds (RE = rare earth metal/actinide; M = transition metal; X = *p*-block element) have attracted a lot of attention over the last decades, as recently acknowledged by the publication of a specific chapter in the Handbook on the Physics and Chemistry of Rare Earths [1]. The main reason at the origin of such an interest can be found in their rich structural chemistry and intriguing physical properties. As a matter of fact, more than 200 $RE_2M_3X_5$ compounds crystallizing with eight different structure types [1,2] have been reported so far, with some representatives displaying noteworthy properties like superconductivity [3–6], Kondo behaviour [7–9] and giant magnetoresistance [10,11]. In selected cases, structural and physical property studies were extended also to pseudoternary $(RE_xRE'_{1-x})_2M_3X_5$ [5,12,13], $RE_2(M_xM'_{1-x})_3X_5$ [12,14,15] and $RE_2M_3(X_xX'_{1-x})_5$ [12] phases, and to the quaternary $RE_2Pt_3Ga_4In$ (RE = Y, Gd–Tm) site ordering variant of the orthorhombic $Y_2Rh_3Sn_5$ type (*Cmc* 2_1) [16]. Over the last ten years, our attention was devoted to studying the crystal structure, chemical bonding, and magnetism of ternary rare-earth germanides [17–20], including the $RE_2Pd_3Ge_5$ series [21–23]. They were detected with RE = La–Nd, Sm, Yb and found to crystallize in all cases with the *oI*40–$U_2Co_3Si_5$ structure type (*Ibam*), which is the most reported one for the $RE_2M_3Ge_5$ germanides together with the structurally related monoclinic *mS*40–$Lu_2Co_3Si_5$ type (*C*2/*c*) [1]. Both the orthorhombic and monoclinic modifications can be derived by symmetry reduction from the $BaAl_4$ (*I*4/*mmm*) aristotype [21]. Considering both our studies conducted on the $RE_2Pd_3Ge_5$ series and the aforementioned literature data, a study about the existence and extent of a solid solution between the $La_2Pd_3Ge_5$ and $La_2Pd_3Si_5$ endmembers was undertaken, also with the aim of verifying the potential formation of ordered quaternary phases. With this purpose, similarly to our investigation on $La_2Pd_3Ge_5$ [23], a comprehensive structural, thermal, and computational study of the $La_2Pd_3Si_5$ endmember was performed, enriching its characterization, previously limited to cell parameters and resistivity measurements [8]. The chemical bonding analysis presented for the $La_2Pd_3Si_5$ compound is followed by a volume chemistry investigation within the quaternary solid solution, enabled by the calculation of atomic volumes according to the Quantum Theory of Atoms in Molecules (QTAIM) [24].

* Corresponding author.
E-mail address: riccardo.freccero@unige.it (R. Freccero).

https://doi.org/10.1016/j.jallcom.2024.174757
Received 22 January 2024; Received in revised form 7 April 2024; Accepted 5 May 2024
Available online 8 May 2024

2. Experimental

2.1. Sample preparation and SEM/EDXS characterization

Samples of nominal composition $La_{20.0}Pd_{30.0}(Si_xGe_{1-x})_{50.0}$ (subscript in at %), with $x = 0.25$, 0.50, 0.70, 0.75 and 1.00, were prepared starting from stoichiometric amounts of the pure elements: lanthanum (ingot, 99.9 %, supplied by Newmet Koch, Waltham Abbey, UK), palladium (foil, 99.95 %, supplied by MaTecK, Jülich, Germany), germanium (chunk, 99.999 %, supplied by Newmet Koch, Waltham Abbey, UK) and silicon (chunk, 99.9999 %, Koch-Light Limited, Haverhill, UK). The constituents were arc melted on a water-cooled copper hearth with a tungsten electrode in Ar atmosphere, obtaining very brittle and air-stable ingots of about 0.8 g; to ensure homogeneity, each ingot was remelted at least three times. Mass losses were less than 1 wt %. Pieces of each ingot were put into an alumina crucible, closed in an evacuated quartz ampoule and annealed at 1000°C for one week prior to water quenching.

$La_2Pd_3Si_5$ single crystals suitable for X-ray diffraction analyses were successfully recrystallized from a tin flux by weighting 0.45 g of the arc-melted ingot, which were ground into fine powders in an agate mortar and inserted in an alumina crucible together with 3.30 g of Sn (1:45 molar ratio). The alumina crucible was subsequently closed in an evacuated quartz tube, hung in a resistance furnace and submitted to the following thermal cycle while rotating at a speed of 100 rpm: 1) heating up to 1050 °C in about 2 h; 2) dwelling at 1050°C for 48 hours; 3) cooling down to 650°C in about 400 hours. Then, the furnace was switched off and opened to extract the samples only after reaching the room temperature.

Obtained $La_2Pd_3Si_5$ crystals were separated from the Sn flux in two steps. First, specimen pieces were sealed in a quartz tube, heated at 500°C, and centrifugated several times at a speed of 600 rpm for 1 min using glass wool as a filter; subsequently, the residual Sn was selectively oxidized by immersion and sonication of the crystals in an aqueous solution of HCl 35 wt % for 10 minutes. The obtained grey and shining crystals were finally washed several times with deionized water, increasing the pH value to 7, and acetone (see Figure S1). Finally, in order to check whether tin had a stabilizing effect on the orthorhombic $La_2Pd_3Si_5$ phase, a piece of the as cast ingot was submitted to the same thermal treatment applied to the Sn-flux specimen.

To perform the metallographic analysis, small pieces of each prepared sample were embedded in a conductive carbon-containing phenolic resin with the aid of the hot compression mounting press Opal 410 (ATM GmbH, Germany). Then a multistep grinding (SiC papers from 600 to 1200 mesh) and polishing (from 6 to 1 μm diamond pastes) procedure was performed using running water and an alcohol-based lubricant respectively, employing the automatic polishing machine Saphir 520 (ATM GmbH, Germany). At the end of each polishing step, sample surfaces were cleaned for a few minutes in an ultrasonic bath using petroleum ether. Some single crystals of $La_2Pd_3Si_5$ separated from the Sn flux were placed on a conductive carbon resin and analysed as such. Microstructure examination as well as semiquantitative elemental analysis were performed using a scanning electron microscope (SEM) Zeiss Evo 40 (Carl Zeiss SMT Ltd., Cambridge, England), equipped with an energy dispersive X-ray (EDX) spectroscope from Oxford Instruments (INCA X-ACT). A cobalt standard was used for calibration.

2.2. X-ray diffraction measurements (XRD) and crystal structure determination

A $La_2Pd_3Si_5$ single crystal was selected among those extracted from Sn-flux, checked by a light optical microscope, and glued to a glass fibre. The X-ray diffraction measurement was performed on a three-circle Bruker D8 QUEST diffractometer equipped by a PHOTON III 14 photon counting detector, using the graphite monochromatized Mo Kα radiation. Data collection strategy, including five ω- and one φ-scan, was proposed by APEX4 software [25] considering data completeness, redundancy, and high resolution limit. Intensity data were collected over the reciprocal space up to ≈ 45° in θ (achieving a resolution of *ca.* 0.5 Å) with exposures of 15 s per frame. Data were reduced using SAINT [26] and XPREP [27]. Lorentz, polarization, and absorption effects were corrected using SADABS [28]. The crystal structure was solved and refined with the aid of SHELXTL [29].

The structural model was easily found by intrinsic phasing algorithm and successively refined using full-matrix least squares methods obtaining excellent residuals. $La_2Pd_3Si_5$ is orthorhombic, isostructural with $La_2Pd_3Ge_5$ [23]. The corresponding CIF file is available in the supporting information material, and it has been deposited at the Cambridge Structural Database. Selected crystallographic data and structure refinement parameters are listed in Table 1.

X-ray powder diffraction (XRPD) measurements were conducted on all samples by means of a Philips *X'Pert* MPD diffractometer with a θ:2θ Bragg-Brentano geometry (Cu *K*α radiation, λ = 1.5406 Å, graphite crystal monochromator, PIXcel^{1D} detector). Powder patterns were collected in the 10°-100° 2θ range in the continuous scan mode. Sample powders were prepared in an agate mortar and loaded in the cavity of a monocrystalline silicon holder designed to minimize background and displacement effects. Rietveld refinements were conducted using the Fullprof [30] software on the powder pattern of samples of nominal composition $La_{20.0}Pd_{30.0}(Si_xGe_{1-x})_{50.0}$, with $x = 0.25$, 0.50, 0.75, 1.00. In all cases, the refinement converged with acceptable residuals (Table 2) and good difference profiles between the observed and calculated patterns leading to chemically meaningful models.

Precise lattice parameters were calculated by least-squares fits with the program LATCON [31]. The same set of (*h k l*) reflections (Table S1) have been selected in all cases to enable the best comparability among different samples. The crystal structure was visualized using the CrystalMaker software [32].

2.3. Differential scanning calorimetry (DSC)

The thermal behaviour of the ternary $La_{20.0}Pd_{30.0}Si_{50.0}$ sample was investigated by differential scanning calorimetry (DSC) using a LABSYS EVO (SETARAM Instrumentation, Caluire, France), equipped with type S (Pt-PtRh 10 %) thermocouples and a DSC holder tray sensor. Measurements were conducted in the temperature range of 20–1550°C with

Table 1
Crystal data and structure refinement details for the $La_2Pd_3Si_5$ single crystal.

Compound	**$La_2Pd_3Si_5$**
CSD code	2252470
Formula weight [g/mol]	737.47
Structural prototype	$U_2Co_3Ge_5$
Pearson symbol	*oI*40
Crystal system	orthorhombic
Space group	*Ibam*
a [Å]	10.0058(10)
b [Å]	11.9096(12)
c [Å]	6.0146(6)
Unit cell volume [Å^3]	716.73(12)
Unit formula per cell, *Z*	4
Calculated density, ρ [g/cm^3]	6.834
Absorption coefficient, μ [mm^{-1}]	19.773
Theta range [°]	$2.7° \leq \vartheta \leq 45.4°$
Index ranges *h*, *k*, *l*	$-17 \leq h \leq 20$
	$-23 \leq k \leq 23$
	$-12 \leq l \leq 12$
Reflections collected	19237
Absorption correction	multi-scan
Data/parameter	1597/31
Goodness of fit on F^2	1.040
Final *R* indices [$I > 2\sigma(I)$]	R1 = 0.0220, wR2 = 0.0412
R indices (all data)	R1 = 0.0309, wR2 = 0.0436
R_{int}/R_{sym}	0.0503/0.0274
Largest diff. peak and hole [e$^-$/Å^3]	3.036 and −2.088

Table 2
Agreement indexes resulting from the Rietveld refinements on $La_2Pd_3(Si_xGe_{1-x})_5$ with x = 0.25, 0.50, 0.75 and 1.00. R_p, R_{wp} and R_B are the profile, weighted profile, and Bragg factors, respectively. χ^2 is defined as the square of the R_{wp}/R_{exp} ratio.

Si content (*x*)	R_p	R_{wp}	R_B	χ^2
0.25	11.3	9.91	3.68	4.66
0.50	11.1	9.81	4.42	5.27
0.75	16.5	14.8	7.34	8.43
1.00	12.2	10.6	4.54	5.84

a heating/cooling rate of 5 °C/min under an Ar flow (20 mL/min). Alumina crucibles were employed both as sample containers and references; pieces of the $La_2Pd_3Si_5$ single-phase sample (~100 mg) annealed at 1000°C for one week (see paragraph 2.1) were used. The recorded thermogram was evaluated and analysed with the aid of the Calisto software [33], provided by SETARAM. To calibrate the instrument, the melting points of standard materials (pure metals: Au, Ge, Cu and Ni) measured at 5 °C/min in alumina crucibles, and their tabulated values [34] were employed.

2.4. Computational techniques

Chemical bonding analysis for ternary $La_2Pd_3Si_5$. The electronic structure of $La_2Pd_3Si_5$ was investigated employing the TB-LMTO-ASA 4.7c software [35], using the Barth and Hedin [36] exchange and correlation potential within the Local Density Approximation (LDA). Experimental crystal structure data obtained in this work from single crystal diffraction experiments were used. The addition of empty spheres to meet the minimum overlapping criterion was not necessary; the following atomic spheres radii were obtained: *r*(La) = 2.146 Å, *r*(Si1) = 1.444 Å, *r*(Si2) = 1.429 Å, *r*(Si3) = 1.431 Å, *r*(Pd1) = 1.383 Å and *r* (Pd2) = 1.443 Å. The self-consistent calculation was performed with a basis set including La-6*s*/(6*p*)/5*d*/4*f*, Si-3*s*/3*p*/(3*d*) and Pd-5*s*/5*p*/4*d*/(4*f*); parentheses indicate orbitals treated according to a downfolding procedure. The *k*-space integration was performed using the tetrahedron method with 280 irreducible *k*-points from a total of 1728. The chemical bonding was studied on the basis of Crystal Orbital Hamilton Populations (COHP) [37] and the corresponding Integrated values up to the Fermi level (ICOHP). Density Of States (DOS) and COHP curves were visualized using wxDragon [38], setting the Fermi energy at 0 eV. A COHP calculation was also performed for elemental *cF*8 silicon and germanium (a_{Si} = 5.431 Å, a_{Ge} = 5.658 Å [2]); basis sets including Si-3*s*/3*p*/(3*d*) and Ge-4*s*/4*p*/(4*d*) were used and the *k*-space was sampled with 104 irreducible *k*-points from a total of 2744.

Volume chemistry within the quaternary $La_2Pd_3(Si_xGe_{1-x})_5$ phase. The quaternary phase $La_2Pd_3(Si_xGe_{1-x})_5$ with x = 0.50 has been simulated with three different structural models. The first two (structure 1 and 2) have been generated by a random distribution of Si and Ge atoms in the 4*a*, 8*g* and 8*j* positions. The last one (structure 3) was generated by distributing Si and Ge in the 8*g* and 8*j* sites so that only Si–Ge contacts occur and in the 4*a* site by alternating Si and Ge along [001]. For all three structures, only the translational symmetry was retained (space group *P*1) using the experimentally determined unit cell parameters. The atomic coordinates for the three quaternary models have been optimized utilizing the all-electron FHI-aims package [39,40] at the DFT/LDA (Perdew and Zunger) [41] level of theory. Predefined default "light" basis set for all atomic species were selected and a (4 4 8) *k*-point mesh was set to sample the Brillouin zone. Scalar relativistic effects were included within the "atomic ZORA" approximation as well as a Gaussian smearing of 0.01 eV. Structure 3 turned out to have a symmetry compatible with the *P*2 space group, whereas both structures 1 and 2 keep a symmetry compatible with the *P*1 space group. The CIF files of relaxed models 1–3 are provided as Supplementary Material. Finally, the electron density (ED) was calculated on an equidistant grid of about 0.05 Bohr for the ternary $La_2Pd_3Si_5$ and the three simulated structures for the quaternary $La_2Pd_3(Si_{0.5}Ge_{0.5})_5$ composition, using an implemented module [42] within the FPLO software [43]. The same exchange and correlation potential applied in the LMTO calculations was employed, sampling the Brillouin zone with an 8×8×8 ($La_2Pd_3Si_5$), 4×4×8 (structures 1 and 2) and 8×4×4 (structure 3) *k*-point mesh. The obtained EDs were analysed within the framework of the Bader's Quantum Theory of Atoms In Molecules (QTAIM) [24] utilizing the DGrid program [44]. In this way, both atomic effective charges (Q^{eff}) and volumes (V^{QTAIM}) are accessible. To check the dependency of the calculated Q^{eff} and V^{QTAIM} to the exchange and correlation functional, an additional PBE calculation was performed for $La_2Pd_3Si_5$. The QTAIM atomic basins were visualized within the unit cells by means of the ParaView suite [45,46]. It is worth noting that the same software programs and computational setup employed to investigate $La_2Pd_3Ge_5$ were chosen for this work, enabling a comparative analysis.

3. Results and discussion

3.1. The $La_2Pd_3Si_5$ endmember

The X-ray powder diffraction pattern of the ternary $La_{20.0}Pd_{30.0}Si_{50.0}$ alloy was indexed (see Fig. 1a) considering the *oI*40-$U_2Co_3Si_5$ structural model, revealing a single-phase sample. Such finding is also corroborated by the SEM/BSE analysis (Fig. 1a, insert), with a measured EDXS composition in line with the 2:3:5 stoichiometry (Table 3). Calculated unit cell parameters (Table 3) are in good agreement with those already reported [1,8].

Three endothermic and three exothermic effects have been detected during DSC heating and cooling measurements, respectively, as shown in Fig. 2.

For the two effects below 1000 °C, the onset temperatures were selected, whereas the peak maxima were considered as the liquidus temperatures, according to the recommendation of Boettinger et al. [47]. Focusing on the heating curve (red line Fig. 2), the effect at 1481°C could be interpreted as the melting of the $La_2Pd_3Si_5$ intermetallic, analogously to the isostructural $La_2Pd_3Ge_5$ compound, which was found to melt congruently at 1058°C [23]. Such a finding is further corroborated by the single-phase nature of the prepared samples after arc melting. The two effects at lower temperatures can be ascribed to some phases and/or microstructural components occurring in an amount below the detection limit of the XRPD, and not observed in the alloy pieces submitted to the SEM investigation. The same effects detected upon heating were also recorded during cooling, with a moderate overcooling for the solidification (1456°C) and the last effect (883°C). SEM/EDXS analysis performed after DSC revealed a single phase $La_2Pd_3Si_5$ sample with composition 19.9 at % La, 31.6 at % Pd, 48.5 at % Si, in perfect agreement with that measured on the annealed sample (Table 3 and Figure S2). It is worth specifying that neither of the lower-temperature effects are to be interpreted as a decomposition or a polymorphic transition of $La_2Pd_3Si_5$. In fact, the powder pattern of a sample submitted to a slow-cooling (1°C/h) thermal treatment down to 650 °C does not show differences from that of the sample annealed at 1000 °C (see Figure S3). Moreover, these findings agree with literature data where $La_2Pd_3Si_5$ with *oI*40-$U_2Co_3Si_5$ crystal structure was reported after annealing at 900 °C [8].

Despite the almost single-phase nature of the prepared samples, it was not straightforward to select good quality crystals for structure solution, also due to twinning. At this point, the recrystallization of $La_2Pd_3Si_5$ in Sn flux enabled the growth of crystals (see Figure S1) of suitable dimension and quality for X-ray structure solution. The obtained unit cell parameters and structural data (Tables 1 and 4) turned out to be in good agreement with those refined from X-ray powder pattern (see Table 3 and S2).

The interatomic distance among the tetrel atoms in the 8*g* and 8*f* sites ($d_{Si2–Si3}$ = 2.495 Å, see Table 5) suggests the presence of Si–Si

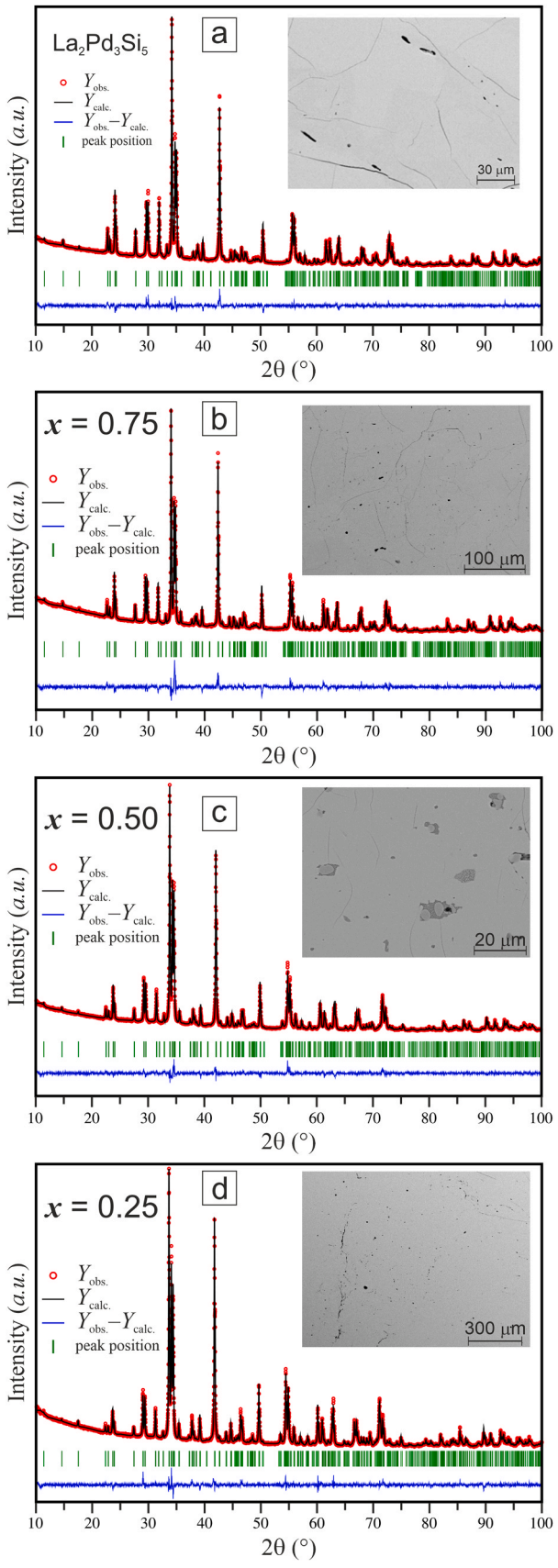

Fig. 1. Rietveld refinement plots and SEM/BSE micrographs (inserts) for the $La_{20.0}Pd_{30.0}(Si_xGe_{1-x})_{50.0}$ samples.

covalent bonds realizing infinite zigzag chains perpendicular to (001), as shown in Fig. 3. On the contrary, the interpretation of the shortest homocontacts for the Si1 atoms ($d_{Si1–Si1}$ = 3.007 Å) as a covalent interaction is not appropriate.

This partial structure composed of covalently two-bonded (2*b*) and isolated (0*b*) Si atoms, formally obeys the Zintl electron count [48], leading to the $(La^{3+})_2(Pd^{2+})_3[(2b)Si^{2-}]_4[(0b)Si^{4-}]$ simplified ionic formula. Nevertheless, in-depth chemical bonding studies performed on binary and ternary tetrelides, have clearly displayed that the complete charge transfer approximation to the *Tt* element has to be abandoned due to polar-covalent interactions, often featuring multicentre/multiatomic character [19,20,49–57]. The very same conclusion was recently drawn after studying the chemical interactions within the isostructural $La_2Pd_3Ge_5$ [23] which comprises, in addition to (2*b*)Ge–(2*b*)Ge homopolar bonds, heteropolar La–Pd and Ge–La/Pd, with the latter displaying a multicentre character. In this work, the chemical bonding in $La_2Pd_3Si_5$ has been inspected and compared to that described for $La_2Pd_3Ge_5$. The resulting bonding picture indicates a similar scenario, as could be initially expected considering either the chemical analogies between Si and Ge, either the isostructural nature of the compounds. Nonetheless, some differences can be pointed out as well. Effective QTAIM charges (Table 5) confirm that Pd atoms get the most negative values, and that La is a cation. Over the last years, the anionic behaviour of palladium, and more generally of certain transition metals, in intermetallic compounds featuring interesting structural [58–66], physical [67,68] and chemical [69–72] properties has been reported. While the Q^{eff}(La) and Q^{eff}(Pd2) are almost identical in the Ge- and Si-containing analogues (La: +1.45 *vs* +1.42, Pd2: –0.62 *vs* –0.59, respectively), the same does not apply to Pd1 displaying a larger absolute value in the actual case (–0.71 *vs* –1.05), although the trend Q^{eff}(Pd1) > Q^{eff}(Pd2) is retained. The comparison gets more intriguing when comparing Ge and Si. In fact, while all Ge atoms are anionic (–0.11 < Q^{eff} < –0.23), the only Si species bearing a negative charge is (2*b*)Si3 (– 0.14) while (2*b*)Si2 is practically neutral (–0.01) and (0*b*)Si1 is even a cation (+0.15). These results can be related to a known exception, although rarely mentioned, to the periodic trend of electronegativity, that Si is less electronegative than Ge (*e.g.* χ_{Si} = 1.90, χ_{Ge} = 2.01 Pauling scale; χ_{Si} = 1.92, χ_{Ge} = 1.99 Allen scale). Anyway, a relevant difference between the effective charges of germanium and silicon is observed only for Q^{eff}(Ge1) and Q^{eff}(Si1) (–0.18 *vs* +0.15), whereas Q^{eff}(Ge2/3) and Q^{eff}(Si2/3) differs by just 0.1. It can be concluded that charge is mainly transferred from La to Pd species, with tiny contribution from Si1 which is indeed surrounded by four Pd1 (2.466 Å). In order to check the dependency of calculated Q^{eff} with the chosen exchange and correlation functional, a PBE simulation was additionally performed leading to analogous values (see Table S3). The total and projected density of states (Fig. 4a) confirms the metallic nature of $La_2Pd_3Si_5$ and shows some typical features of ternary rare-earth tetrelides [17,50,52,57,73]: Si 3*s* states dominating the energy region below 7 eV, occupied La 5*d* states, filled Pd 4*d* with a quite wide (~ 3 eV) bandwidth, relevant mixing between Si 3*p*, Pd 4*d* and La 5*d* states. The latter may be ascribed to Si–La/Pd interactions.

To shed more light on the chemical bonding, COHP curves (Fig. 4b-f and S4) and ICOHP values (Table 5) have been calculated and analysed. The covalent nature of bonded chains formed by alternating Si2 and Si3 is confirmed by the corresponding –ICOHP of 2.24 eV. The –COHP curves for Si–Si interactions are mainly positive in the considered energy range (Figs. 4c and 4d); in particular, they are almost optimized at E_F for Si3 and display only a few antibonding states from about −1–0 eV for Si2. Such difference between the two Si may be ascribed to their different coordination environment. In fact, Si3 (Fig. 4d) does not show any homocontact at 2.5 Å < *d* < 3.6 Å (see Table 5), so that only the –COHP curve for Si atoms within the zigzag chains are displayed. The responsible for the antibonding states in the vicinity of E_F for Si2 (Fig. 4c) are the two Si2 and the Si1 atoms at 3.007 and 3.235 Å, respectively, which only poorly interact as confirmed by the low

Table 3
Results of the SEM/EDXS and XRPD characterizations of the $La_{20.0}Pd_{30.0}(Si_xGe_{1-x})_{50.0}$ samples annealed at 1000°C for 1 week.

x	EDXS composition [at %]				Lattice parameters [Å]			Cell volume [Å^3]
	La	Pd	Si	Ge	*a*	*b*	*c*	*V*
1.00	19.9(1)	31.8(9)	48.3(9)	–	10.0048(6)	11.910(1)	6.0145(4)	716.70(6)
0.75	20.0(2)	30.7(4)	37.0(2)	12.3(4)	10.0468(6)	11.990(1)	6.0594(4)	729.95(6)
0.70	20.0(3)	31.1(6)	33.9(2)	15.0(5)	10.0521(8)	12.017(1)	6.0688(6)	733.09(8)
0.50	20.0(3)	30.8(3)	24.4(3)	24.8(4)	10.0878(6)	12.077(1)	6.1071(4)	744.02(6)
0.25	20.0(2)	30.8(5)	12.5(5)	36.7(5)	10.1316(8)	12.158(2)	6.1494(6)	757.48(9)

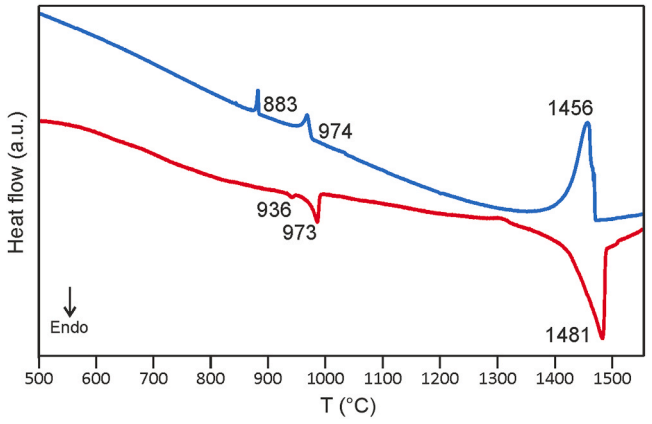

Fig. 2. Measured DSC heating (red) and cooling (blue) curves for the ternary $La_{20.0}Pd_{30.0}Si_{50.0}$ sample.

Table 4
Standardized atomic coordinates and equivalent displacement parameters (U_{eq}) for the $La_2Pd_3Si_5$ single crystal.

Atom	Site	Atomic coordinates			U_{eq} [Å^2]
		x/a	*y/b*	*z/c*	
La	8*j*	0.26375(2)	0.37236(2)	0	0.00574(3)
Pd1	8*j*	0.10853(2)	0.13648(2)	0	0.00689(4)
Pd2	4*b*	1/2	0	1/4	0.00799(5)
Si1	4*a*	0	0	1/4	0.00701(17)
Si2	8 *g*	0	0.27162(7)	1/4	0.00735(12)
Si3	8*j*	0.35361(8)	0.11513(7)	0	0.00696(13)

–ICOHP (0.43 and 0.21 eV). An analogous scenario is observed for Si1 displaying, in addition to the just mentioned two Si2 at 3.235 Å, also two Si1 at 3.007 Å with a –ICOHP of 0.52 eV. These considerations on Si–Si interactions confirm that only the Si atoms within the zigzag chains are considerably covalently bonded so that, limited to homocontacts, the description of Si1 as (0*b*) and of Si2 and Si3 as (2*b*) seems still appropriate. At this point some comparisons with $La_2Pd_3Ge_5$ can be performed. Despite the analogous shape for Si–Si and Ge–Ge –COHP curves [23], the integrated values are rather different, with a –ICOHP between Ge2 and Ge3 of 1.73 eV [23]. The same trend is observed for elemental *cF*8 silicon and germanium with –ICOHP values of 3.63 for Si and of 3.21 eV for Ge. Interestingly, the difference between the –ICOHPs in the elements is 0.42 eV whereas for the $La_2Pd_3Tt_5$ (*Tt*: Si, Ge) intermetallics it ascertains at 0.51 eV. This chemical bonding result can account for the difference in melting temperatures of $La_2Pd_3Si_5$ (1481°C, Fig. 2) and $La_2Pd_3Ge_5$ (1058°C [23]). It is worth underlying that the ICOHP values are not bond strength values but can be considered to somewhat hint toward it. Keeping that in mind and anticipating that the other –ICOHP values are quite similar to those reported for $La_2Pd_3Ge_5$, the higher melting temperature detected for $La_2Pd_3Si_5$ can be mainly ascribed to the Si–Si covalent interactions, as for the pure elements (T_m(Si) = 1410°C, T_m(Ge) = 938°C).

Coming back to the –COHP for Si2 and Si3, the lack of antibonding states with respect to those expected for the formal (2*b*)Si^{2-} Zintl polyanion was also reported for Ge2 and Ge3 in $La_2Pd_3Ge_5$, and related to polar-covalent bonds with the surrounding metals. The same conclusion can be drawn also for the actual case and becomes evident when looking at the Si–Pd and Si–La –(I)COHPs. In fact, the curves for Si–Pd (Fig. 4b-f) are bonding in almost the whole energy range, featuring a nonbonding or weakly antibonding character from −3 up to 0 eV; the –ICOHPs for such bonding ranges from 2.31 eV to 2.01 eV when 2.456 Å< d_{Pd-Si} < 2.507 Å, and gets a value of 1.22 eV (Pd2–Si2) when the distance is increased to 2.720 Å. Thus, Si–Pd covalent interactions are the strongest together with the Si–Si ones. The curves representing Si–La interactions are always bonding in the considered energy window and never saturated at the E_F, displaying bonding states also well-above 0 eV; their integrated COHPs, albeit lower than the Si–Pd ones (0.75 – 1.01 eV), may be still interpreted as an indication of covalent bonding. The presence of these unfilled bonding states together with the observation that silicon atoms interact covalently with a larger number of metals than the number of 2*c*-2*e* bonds they could establish, net of the Si-Si bonds, suggests a multicenter character for Si–Pd/La interactions. Finally, the bonding nature of La–Pd polar interactions is indicated by positive and practically optimized –COHP curves at the E_F (Fig. 4e/f and Figure S4). Thus, as previously anticipated, it can be concluded that a chemical scenario like the one of $La_2Pd_3Ge_5$ is realized.

In conclusion, it has to be noted that Pd2 homocontacts are realized at $d_{Pd2-Pd2}$ of 3.007 Å, slightly shorter than in $La_2Pd_3Ge_5$ ($d_{Pd2-Pd2}$ = 3.095 Å); the shorter distance may be considered responsible for the moderately higher –ICOHP value: 0.66 *vs* 0.58 eV. To correctly interpret this value, a comparison with Ca_2Pd_2Ge [58], Sr_2Pd_2Al [74] and Eu_2Pd_2Sn [75], where the formation of one-dimensional linear Pd chains was claimed, may be helpful. The following values were reported: d_{Pd-Pd} = 2.872 Å, −ICOHP = 0.99 eV for Ca_2Pd_2Ge; d_{Pd-Pd} = 3.031 Å, −ICOHP = 0.84 eV for Sr_2Pd_2Al; d_{Pd-Pd} = 3.002 Å, −ICOHP = 0.85 eV for Eu_2Pd_2Sn. Interestingly, the d_{Pd-Pd} is almost identical in Eu_2Pd_2Sn and $La_2Pd_3Si_5$, with an integrated value lowered of 0.19 eV for the title phase where then the Pd atoms can be considered as weakly interacting.

3.2. The $La_2Pd_3(Si, Ge)_5$ complete solid solution

The X-ray powder diffraction patterns of the quaternary $La_{20.0}Pd_{30.0}(Si_xGe_{1-x})_{50.0}$ alloys (x = 0.75, 0.50, 0.25) were all indexed considering the *oI*40-$U_2Co_3Si_5$ structural model, suggesting the formation of a complete $La_2Pd_3(Si_xGe_{1-x})_5$ ($0 \le x \le 1$) solid solution (Table 3). As for $La_2Pd_3Si_5$, all annealed samples turned out to be single-phase (see Fig. 1b, c, d). The crystal structures of $La_2Pd_3(Si_xGe_{1-x})_5$ were refined using the Rietveld method and the obtained structural data are listed in Table 6.

For the sample with x = 0.75 the occupancies of the Si/Ge sites were fixed to avoid discrepancies between the refined and EDX measured composition (Table 3), resulting in slightly larger agreement factors with respect to the other samples (Table 2).

Both unit cell parameters and volumes display a linear variation as a function of the composition within the solid solution (see Figure S5), revealing trends in line with the empirical Vegard's and Biltz-Zen's rules [76–79]. More in details, the former calls for linear variation of lattice spacing (or of interatomic distances) whereas the latter of volumes,

Table 5
$La_2Pd_3Si_5$ interatomic distances (< 3.6 Å), Integrated Crystal Orbital Hamilton Population (ICOHP) and QTAIM effective charges (Q^{eff}) for each species.

Central atom/ Q^{eff}	Adjacent atoms	*d* (Å)	–ICOHP (*eV/bond*)	Central atom	Adjacent atoms	*d* (Å)	–ICOHP (*eV/bond*)
La (*8j*)	Si3	3.1207(9)	1.01	**Si1 (*4a*)**	Pd1(x4)	2.4662(2)	2.21
+1.42	Si1(x2)	3.1874(2)	0.93	**+0.15**	Si1(x2)	3.0073(4)	0.52
	Si3	3.1927(9)	0.90		La(x4)	3.1874(2)	0.93
	Pd1	3.2100(3)	0.71		Si2(x2)	3.2349(8)	0.23
	Si3 (x2)	3.2319(3)	0.82	**Si2 (*8 g*)**	Pd1(x2)	2.4557(6)	2.25
	Si2(x2)	3.2657(4)	0.81	**–0.01**	Si3(x2)	2.4951(8)	2.24
	Pd1(x2)	3.2693(1)	0.69		Pd2	2.7199(8)	1.22
	Si2(x2)	3.2847(5)	0.75		Si2(x2)	3.0073(4)	0.43
	Pd1	3.3952(3)	0.57		Si1	3.2349(8)	0.23
	Pd2(x2)	3.3965(2)	0.62		La(x2)	3.2657(4)	0.81
	Pd1	3.4514(3)	0.49		La(x2)	3.2847(5)	0.75
Pd1 (*8j*)	Si2(x2)	2.4557(6)	2.25	**Si3 (*8j*)**	Pd1	2.4654(8)	2.31
–1.05	Si3	2.4654(8)	2.31	**–0.14**	Si2(x2)	2.4951(8)	2.24
	Si1(x2)	2.4662(2)	2.21		Pd2(x2)	2.5073(7)	2.01
	La	3.2100(3)	0.71		La	3.1207(9)	1.01
	La(x2)	3.2693(1)	0.69		La	3.1927(9)	0.90
	La	3.3952(3)	0.57		La(x2)	3.2319(3)	0.82
	La	3.4514(3)	0.49				
Pd2 (*4b*)	Si3(x4)	2.5073(7)	2.01				
–0.59	Si2(x2)	2.7199(8)	1.22				
	Pd2(x2)	3.0073(4)	0.66				
	La(x4)	3.3965(2)	0.62				

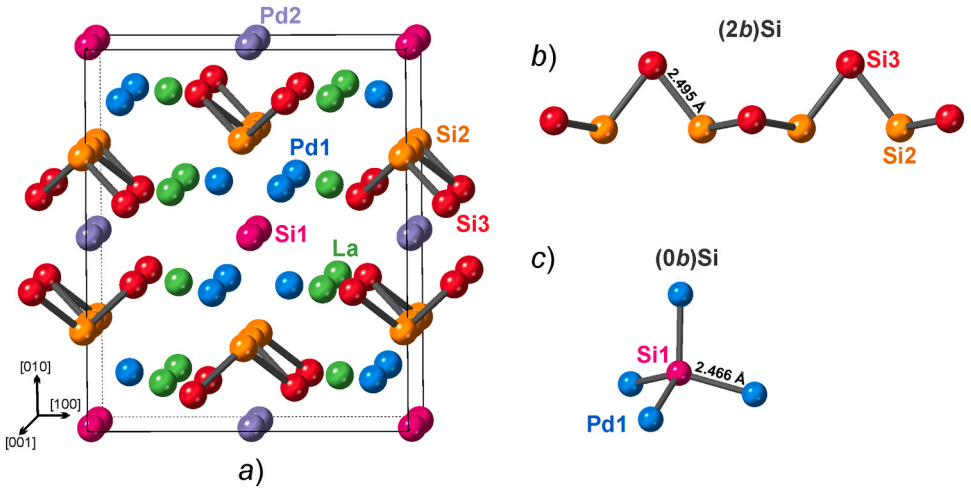

Fig. 3. Crystal structure of $La_2Pd_3Si_5$ with Si–Si covalent interactions indicated by grey sticks (a); (2*b*)Si polyanionic chain (b) and Pd neighbouring atoms of (0*b*)Si species (c).

although in the literature they both typically go under the name of Vegard's rule. Considering that it is well-known that they are rarely obeyed already in binary systems [79,80] the here presented quaternary solid solution represents a quite interesting case. Both the cell parameters and volumes can be calculated starting from the same values for the ternary endmembers for whatever Si content *x*, according to the following equations:

$$a(x) = x a_{La_2Pd_3Si_5} + (1-x) a_{La_2Pd_3Ge_5} \quad (1)$$

$$V(x) = x V_{La_2Pd_3Si_5} + (1-x) V_{La_2Pd_3Ge_5} \quad (2)$$

with the equation for $b(x)$ and $c(x)$ being analogue to that for $a(x)$. The fact that the endmembers are isostructural and exhibit a highly similar bonding scenario, as described in paragraph 3.1, are factors that promote the formation of such a solution, in accordance with the Hume-Rothery rules for binary substitutional solid solutions. A more thorough analysis of the linear volume variation, specifically the average volume per atom $\overline{V}_{at}$ (Fig. 5a, black dashed line), can be conducted by examining the QTAIM volumes (V^{QTAIM}) with the purpose to assess and relate the origin of the $\overline{V}_{at}$ variation to atomic quantities.

This approach was first applied to metal nitrides and hydrides [81–84], enabling to find for binary compounds a linear relation between QTAIM atomic volumes and those derived from tabulated Biltz's volume increments [77]. Subsequently, such a technique was used to introduce the variation of atomic volumes with composition in binary systems comprising metals, leading to an extension of the Vegard's approach [83,85–87]. As a result, non-linear and even non-monotonic slopes of the atomic volumes as a function of the concentration are obtained and can be used to qualitatively explain the experimentally observed trends. These systematic QTAIM analyses have been conducted for all intermetallics within the Al-Pt [85], Y-Ga [86] and Be-Ru [87] systems. Volume deviations from linearity have been elucidated through chemical bonding studies, displaying polar covalent interactions among the constituents, often featuring a multi-atomic nature. It is worth noting that in the mentioned cases, QTAIM volumes were used to investigate Vegard's deviation in binary systems where complete solid solubility is absent and numerous intermetallics form. In this study, the same approach is used and applied for the first time to an extended quaternary solid solution. With this purpose, in addition to the V^{QTAIM} for $La_2Pd_3Si_5$

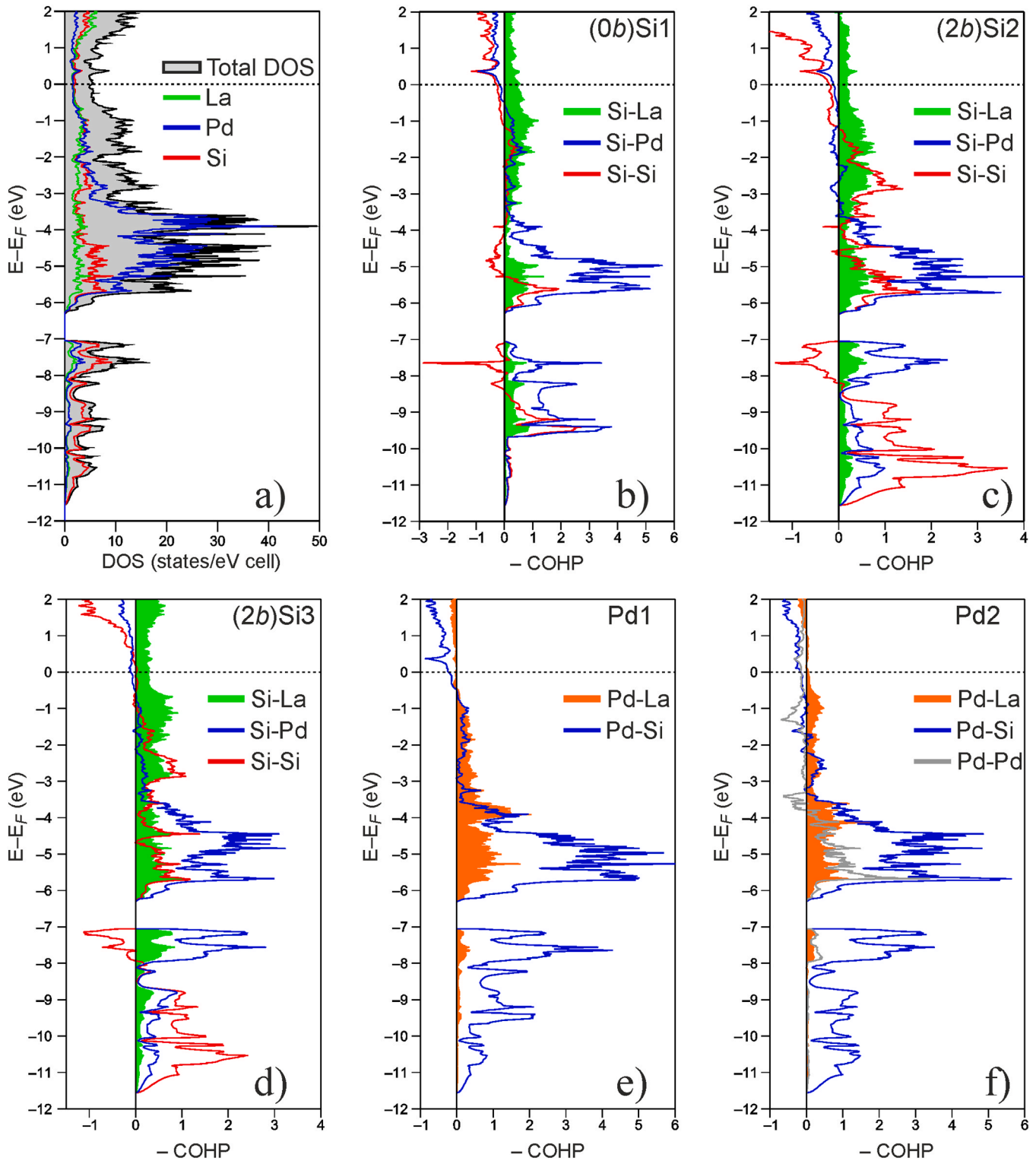

Fig. 4. (a) Total and atom-projected Density Of States (*p*)DOS for $La_2Pd_3Si_5$ together with cumulative Crystal Orbital Hamilton Population curves (−COHP) for the interactions between (b) Si1, (c) Si2, (d) Si3, (e) Pd1 and (f) Pd2 with the atoms of their coordination environments.

(this work) and for $La_2Pd_3Ge_5$ [23], those for the $La_2Pd_3(Si_{0.5}Ge_{0.5})_5$ phase, simulated by three structural models, have been used. Selected QTAIM basins for the model labelled as "structure 1" are displayed in Fig. 6.

It is interesting to note that low energy differences are obtained between the simulated structures. More in details, structures 1 and 2 exhibit similar energies ($E(1) - E(2) = -0.8 meV/at$) which are both slightly lower than that of the more symmetric structure 3 ($E(1) - E(3) = -5.0 meV/at$); this aligns with the experimental data, where no ordering indications were detected, and supports the employed models. The values of V^{QTAIM} both for each atom in the unit cells and averaged over species of the simulated quaternary phases are listed in Tables S4 and S5, respectively.

The change of QTAIM atomic volumes as a function of the Si content

Table 6
Standardized atomic coordinates and equivalent isotropic displacement parameters for the $La_2Pd_3(Si_xGe_{1-x})_5$ phases with $x = 0.25$, 0.50 and 0.75.

Atom	Site	Atomic coordinates			SOF ≠ 1	B_{eq} [Å^2]
		x/a	*y/b*	*z/c*		
$x = 0.25$						
La	8*j*	0.2650(1)	0.3696(1)	0		1.07(4)
Pd1	8*j*	0.1073(1)	0.1391(1)	0		1.17(5)
Pd2	4*b*	½	0	¼		1.62(7)
Si1	4*a*	0	0	¼	0.14(1)	1.16(11)
Ge1					0.86(1)	
Si2	8 *g*	0	0.2747(1)	¼	0.28(1)	1.32(9)
Ge2					0.72(1)	
Si3	8*j*	0.3490(1)	0.1075(1)	0	0.31(1)	1.66(8)
Ge3					0.69(1)	
$x = 0.50$						
La	8*j*	0.2647(1)	0.3714(1)	0		1.16(8)
Pd1	8*j*	0.1082(1)	0.1393(1)	0		1.70(4)
Pd2	4*b*	½	0	¼		2.20(3)
Si1	4*a*	0	0	¼	0.36(1)	1.12(10)
Ge1					0.64(1)	
Si2	8 *g*	0	0.2716(1)	¼	0.52(1)	2.02(5)
Ge2					0.48(1)	
Si3	8*j*	0.3452(1)	0.1090(1)	0	0.55(1)	1.56(6)
Ge3					0.45(1)	
$x = 0.75$						
La	8*j*	0.2637(1)	0.3721(1)	0		1.49(6)
Pd1	8*j*	0.1093(1)	0.1376(1)	0		1.55(7)
Pd2	4*b*	½	0	¼		1.43(1)
Si1	4*a*	0	0	¼	0.75	0.54(2)
Ge1					0.25	
Si2	8 *g*	0	0.2697(1)	¼	0.75	2.44(2)
Ge2					0.25	
Si3	8*j*	0.3359(1)	0.1148(1)	0	0.75	1.40(1)
Ge3					0.25	

x is well represented for each species by a linear regression (Fig. 5a), and can be viewed as an extension to quaternary systems of the scheme suggested by Baranov et al. [85] for Vegard-like trends. Thus, Eq. 2 can be expressed in relation to the atomic volumes:

$$V(x) = x\sum_{\Omega} w_\Omega V_{\Omega_{La2Pd3Si5}} + (1-x)\sum_{\Omega} w_\Omega V_{\Omega_{La2Pd3Ge5}} \quad (3)$$

with Ω indicating QTAIM atomic species, w_Ω the multiplicity of the Wyckoff position occupied by atom Ω, V_Ω the QTAIM volume of atom Ω in $La_2Pd_3Si_5$ or $La_2Pd_3Ge_5$. Thus, also the slope of the line obtained from the experimental data, m_{exp} in the following, (black and dashed in Fig. 5a), which is equal to −1.34, can be derived from a weighted arithmetic mean of the atomic ones (see Appendix):

$$m_{exp} = \frac{\sum_{\Omega} w_\Omega m_\Omega}{\sum_{\Omega} w_\Omega} \quad (4)$$

with m_Ω being the slope of the line for atom Ω. The denominator adds up to the number of atoms in the unit cell, *i.e.* 40. Observing the lines in Fig. 5a it is clear that the atoms responsible for the volume contraction moving from $La_2Pd_3Ge_5$ to $La_2Pd_3Si_5$ are the three *Tt* species and La as the lines for Pd1 and Pd2 are nearly parallel to the *x*-axis ($m_{Pd} \sim 0$). In fact, by calculating m_{exp} (Eq. 4) approximating both m_{Pd1} and m_{Pd2} to zero, a slope almost equal to the experimental one is obtained (-1.32). Even without resorting to quantum-chemical calculations, it would have been reasonable to hypothesize that the volume of *Tt* reduces when substituting Ge with Si; the same does not hold for La. In fact, the use of a tabulated radius for La cannot give any hints toward its contraction. The relevance of such a behaviour gets clearer when calculating the m_{exp} (Eq. 4) assuming a flat La line ($m_{La} = 0$), leading to a slope of −1.12 far from the −1.34 value.

The variation of atomic charges as a function of *x* (Fig. 5b) shows a different trend compared to the volumes. In fact, the lines for all species

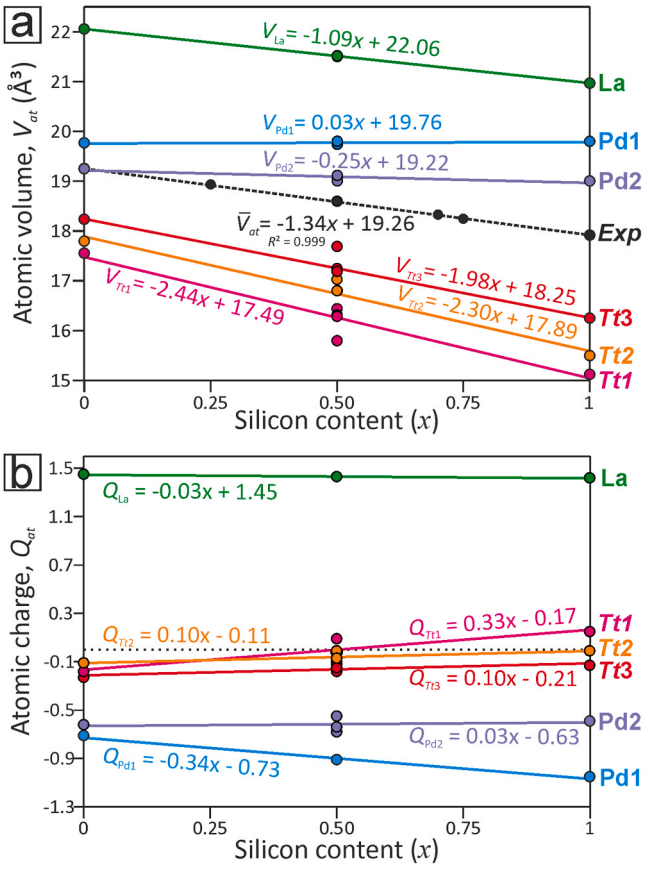

Fig. 5. Experimentally determined average atomic volumes $\overline{V}_{at}$ (black dashed line) and calculated average QTAIM atomic volumes (a) and charges (b) for each species (coloured lines) as a function of the Si content (*x*) within the quaternary $La_2Pd_3(Si_xGe_{1-x})_5$ solid solution. Dotted black line in (b) is a guide to the eye for zero charge. The colouring scheme for atomic species is the same as in Fig. 3.

are almost flat with the exception of Pd1 and *Tt*1. This trend corroborates what was previously mentioned when comparatively discussing Q^{eff} for $La_2Pd_3Ge_5$ and $La_2Pd_3Si_5$ (see paragraph 3.1). The trends of Pd1 and La do not show an immediate correlation between charge and volume. In fact, although the charge of Pd1 decreases its volume keeps constant; conversely, the volume of La displays a contraction while its charge remains between +1.45 and +1.42. These results reveal that, at least for the considered solid solution, there is not a direct relation between charges and volumes so that they should be both investigated in this kind of studies without easily approximating that a charge increase/reduction leads to a volume contraction/expansion.

4. Conclusions

The quaternary complete solid solution $La_2Pd_3(Si_xGe_{1-x})_5$ ($0 \le x \le 1$) is realized between the $La_2Pd_3Ge_5$ and $La_2Pd_3Si_5$ endmembers. Investigated samples at different Si content (*x*) all crystallize with the *oI*40 – $U_2Co_3Si_5$ type structure. Unit cell parameters and volumes change linearly with the Si/Ge ratio displaying a Vegard behavior. QTAIM atomic volumes, calculated for the ternary endmembers and $La_2Pd_3(Si_{0.5}Ge_{0.5})$, suggest that the experimentally observed linear trend is not only due to the substitution of Ge with Si, and vice versa, but also influenced by lanthanum. Interestingly, the La volume change with composition is not correlated with a QTAIM charge variation, suggesting the need for careful consideration when assuming that a charge increase or reduction induces a volume contraction or expansion in these types of investigations.

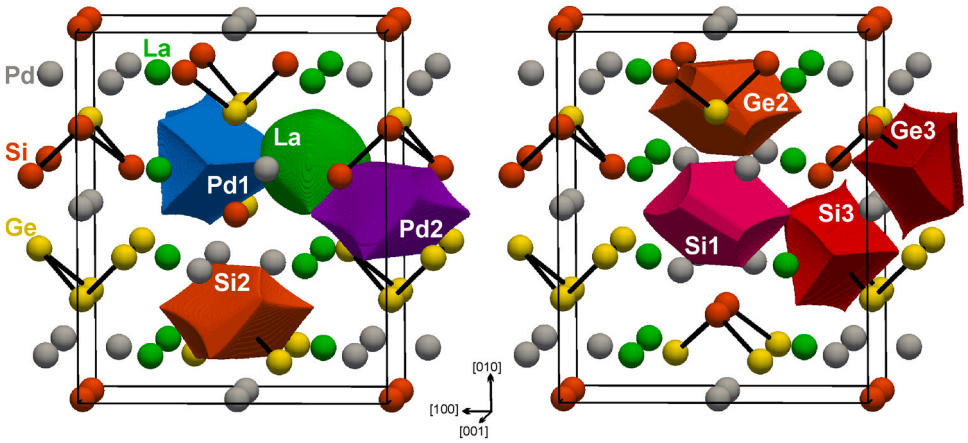

Fig. 6. Shapes of selected QTAIM atomic basins within the unit cell of $La_2Pd_3(Si_{0.5}Ge_{0.5})_5$ (structure 1), chosen as a representative.

This research is further complemented by an experimental and computational study on $La_2Pd_3Si_5$. It shows a bonding pattern similar to $La_2Pd_3Ge_5$, comprising Si–Pd/La multicenter interactions together with La–Pd and Si–Si covalent bonding, with the latter considered the main responsible for its higher melting point with respect to the Ge-analogue.

Finally, we believe these results constitute a good basis to investigate physical property changes as a function of the volume and to tune them together with composition within extended solid solutions for other $RE_2M_3(Si,Ge)_5$ phases, analogously to what has been already described for other compounds; this is for instance the case for the band gap of Cu(Ga, In)Se_2 [88,89]. Moreover, they can be useful to drive the preparation of phononic reference $La_2Pd_3(Si,Ge)_5$ phases, allowing to obtain magnetic contribution to, for instance, the specific heat and the electrical resistivity. Finally, the QTAIM volume analysis undertaken in this work is not specific for intermetallic phases but can be also extended to other classes of materials such as minerals, for which quaternary or even multinary solid solutions are quite common [90–92].

CRediT authorship contribution statement

Serena De Negri: Writing – review & editing, Investigation, Data curation. **Pavlo Solokha:** Writing – review & editing, Investigation, Data curation. **Riccardo Freccero:** Writing – review & editing, Writing – original draft, Software, Methodology, Investigation, Data curation, Conceptualization.

Declaration of Competing Interest

The authors declare that they have no known competing financial interests or personal relationships that could have appeared to influence the work reported in this paper.

Data Availability

Data will be made available on request.

Acknowledgements

The authors thank B.Sc. Giulia Repetto for her contribution to this research in an early stage.

Supporting Information Available

X-ray crystallographic file in CIF format for $La_2Pd_3Si_5$; simulated structural models (1−3) for $La_2Pd_3(Si_{0.5}Ge_{0.5})_5$ in CIF format; SEM/SE micrograph of a $La_2Pd_3Si_5$ single crystals recrystallized in Sn flux (Figure S1); Set of (*h k l*) peaks selected for precise calculation of unit cell parameters (Table S1); SEM/BSE micrograph of the $La_{20.0}Pd_{30.0}Si_{50.0}$ sample after the DSC measurement (Figure S2); X-ray powder patterns for the $La_{20.0}Pd_{30.0}Si_{50.0}$ sample annealed at 1000°C and submitted to a slow-cooling (1°C/h) thermal treatment down to 650 °C (Figure S3); Structural data for $La_2Pd_3Si_5$ obtained from Rietveld refinement (Table S2); QTAIM effective charges and atomic volumes for $La_2Pd_3Si_5$ obtained from a DFT/PBE calculation (Table S3); COHP curves for the interactions between La and the atoms in its coordination environment (Figure S4); linear trend of unit cell parameters and volumes as a function of the Si content for $La_2Pd_3(Si_xGe_{1-x})_5$ (Figure S5); QTAIM volumes and charges for each atom and averaged (Table S4 and S5).

Appendix

If a substitutional solid solution between two crystalline and isostructural endmembers A and B is formed, A_xB_{1-x}, and shows a linear change of the unit cell volume as a function of the composition *x*, the following equation is found from experimental data:

$$V(x) = xm_{exp} + q_{exp} \tag{5}$$

The subscript "*exp*" indicate that both the slope *m* and the *y*-intercept *q* are obtained from a linear regression on experimentally obtained volumes *V* (*x*) and compositions *x*. It is worth underlying that the endmembers A and B do not need to be elements and might be formed by whatever number of elements. Nevertheless, in the present discussion, the substitution along the solid solution has to occur only between two elements, with their relative content expressed by *x*. For example, in this study A and B are $La_2Pd_3Si_5$ and $La_2Pd_3Ge_5$, respectively. The well-known formulation of the Vegard law can be derived from Eq. 5 by substituting:

$$m_{exp} = \frac{V_A - V_B}{1 - 0};\ q_{exp} = V_B \tag{6}$$

leading to:

$$V(x) = xV_A + (1 - x)V_B \tag{7}$$

Since the endmembers A and B are constituted by atoms Ω occupying Wyckoff sites of multiplicity w_Ω, the unit cell volumes of each of them can be expressed with the following sum of QTAIM atomic volumes V_Ω:

$$V_A = \sum_\Omega w_\Omega V_{\Omega_A}; V_B = \sum_\Omega w_\Omega V_{\Omega_B} \quad (8)$$

Eq.7 becomes:

$$V(x) = x\sum_\Omega w_\Omega V_{\Omega_A} + (1-x)\sum_\Omega w_\Omega V_{\Omega_B} \quad (9)$$

In this study, Eq. 9 corresponds to Eq. 3 (A = $La_2Pd_3Si_5$; B = $La_2Pd_3Ge_5$).

In the Vegard case also the QTAIM atomic volumes are expected to change linearly with composition:

$$V_\Omega(x) = xm_\Omega + q_\Omega \quad (10)$$

Thus, Eq. 5 can be expressed as follow:

$$V(x) = x\sum_\Omega w_\Omega m_\Omega + \sum_\Omega w_\Omega q_\Omega \quad (11)$$

If the volume per atom is considered, it is sufficient to divide the left- and right-hand sides by the number of atoms in the unit cell, i.e. $\sum_\Omega w_\Omega$, obtaining m_{exp} according to Eq. 4.

Appendix A. Supporting information

Supplementary data associated with this article can be found in the online version at doi:10.1016/j.jallcom.2024.174757.

References

[1] W.K. Brown, M.A. Plata, M.E. Raines, J.Y. Chan, Structural and physical properties of $R_2M_3X_5$ compounds, Handb. Phys. Chem. Rare Earths. (2023), https://doi.org/10.1016/BS.HPCRE.2023.09.001.

[2] P. Villars, K. Cenzual, Pearson's Crystal Data: Crystal Structure Database for Inorganic Compounds, Release 2022/23, ASM International, Materials Park, Ohio, USA.

[3] H.F. Braun, Superconductivity of rare earth-iron silicides, Phys. Lett. A. 75 (1980) 386–388, https://doi.org/10.1016/0375-9601(80)90849-X.

[4] C. Mazumdar, K. Ghosh, S. Ramakrishnan, R. Nagarajan, L.C. Gupta, G. Chandra, B. D. Padalia, R. Vijayaraghavan, Superconductivity in the ternary nickel silicide $Lu_2Ni_3Si_5$, Phys. Rev. B. 50 (1994) 13879, https://doi.org/10.1103/PhysRevB.50.13879.

[5] N.G. Patil, K. Ghosh, S. Ramakrishnan, Study of superconductivity and antiferromagnetism in $La_{2-x}Nd_xRh_3Si_5$ system, Phys. B Condens. Matter 223–224 (1996) 392–395, https://doi.org/10.1016/0921-4526(96)00132-9.

[6] Y. Singh, S. Ramakrishnan, Magnetic ordering and superconductivity in the $R_2Ir_3Ge_5$(R=Y, La, Ce-Nd, Gd-Tm, Lu) system, Phys. Rev. B. 69 (2004) 174423, https://doi.org/10.1103/PhysRevB.69.174423.

[7] M. Abliz, M. Hedo, J. Kitagawa, Y. Uwatoko, M. Ishikawa, Pressure induced Kondo coherence effect in $Ce_2Pd_3Si_5$, J. Alloy. Compd. 408–412 (2006) 241–243, https://doi.org/10.1016/J.JALLCOM.2005.04.029.

[8] D. Huo, J. Sakurai, T. Kuwai, T. Mizushima, Y. Isikawa, Antiferromagnetism in the Kondo lattice compound $Ce_2Pd_3Si_5$, Phys. Rev. B 65 (2002) 144450, https://doi.org/10.1103/PhysRevB.65.144450.

[9] Z. Hossain, H. Ohmoto, K. Umeo, F. Iga, T. Suzuki, T. Takabatake, N. Takamoto, K. Kindo, Antiferromagnetic Kondo-lattice systems $Ce_2Rh_3Ge_5$ and $Ce_2Ir_3Ge_5$ with moderate heavy-fermion behavior, Phys. Rev. B 60 (1999) 10383, https://doi.org/10.1103/PhysRevB.60.10383.

[10] C. Mazumdar, A.K. Nigam, R. Nagarajan, C. Godart, L.C. Gupta, B.D. Padalia, G. Chandra, R. Vijayaraghavan, Positive giant magnetoresistance in antiferromagnetic $RE_2Ni_3Si_5$ (RE=Tb, Sm, Nd), Appl. Phys. Lett. 68 (1996) 3647–3649, https://doi.org/10.1063/1.115758.

[11] R. Nirmala, S.K. Malik, A.V. Morozkin, Y. Yamamoto, H. Hori, Large magnetoresistance in intermetallic compounds $R_2Mn_3Si_5$ (R = Tb, Dy and Ho), Europhys. Lett. 76 (2006) 471, https://doi.org/10.1209/EPL/I2006-10290-6.

[12] N.S. Sangeetha, A. Thamizhavel, C.V. Tomy, S. Basu, A.M. Awasthi, S. Ramakrishnan, D. Pal, Interplay of superconductivity and charge density wave ordering in pseudoternary alloy compounds: $Lu_2Ir_3(Si_{1-x}Ge_x)_5$, $Lu_2(Ir_{1-x}Rh_x)_3Si_5$, and $(Lu_{1-x}Sc_x)_2Ir_3Si_5$, Phys. Rev. B - Condens. Matter Mater. Phys. 86 (2012) 024524, https://doi.org/10.1103/PhysRevB.86.024524.

[13] R. Khan, K. Althubeiti, M. Algethami, N. Rahman, M. Sohail, Q. Mao, Q. Zaman, A. Ullah, N. Ilyas, A. Mohammad Afzal, A. Khan, M. Akif Safeen, A. Khan, Observation of quantum criticality in antiferromagnetic based $(Ce_{1-x}Y_x)_2Ir_3Ge_5$ Kondo-Lattice system, J. Magn. Magn. Mater. 556 (2022) 169361, https://doi.org/10.1016/J.JMMM.2022.169361.

[14] C. Rizzoli, O.L. Sologub, P.S. Salamakha, Single crystal investigation of $Sm_2(Ru, Os)_3Si_5$, J. Alloy. Compd. 337 (2002) L4–L7, https://doi.org/10.1016/S0925-8388(01)01937-5.

[15] Y. Xu, R.N. Shelton, The effect of transition metal substitutions for Fe on the magnetic susceptibility of compounds $Lu_2(Fe_{1-x}T_x)_3Si_5$ (T = Cr, Mn, Co, Ni, Cu, Ru), Solid State Commun. 68 (1988) 399–403, https://doi.org/10.1016/0038-1098(88)90303-1.

[16] M. Horiacha, M.K. Reimann, J. Kösters, V. Zaremba, R. Pöttgen, Quaternary intermetallics $RE_2Pt_3Ga_4In$ (RE=Y, Gd-Tm)-intergrowth structures of $NdRh_2Sn_4$ and TiNiSi related slabs, Z. Fur Krist. - Cryst. Mater. 235 (2020) 117–125, https://doi.org/10.1515/zkri-2020-0012.

[17] P. Solokha, S. De Negri, D.M. Proserpio, V.A. Blatov, A. Saccone, Vacancy ordering as a driving factor for structural changes in ternary germanides: the new $R_2Zn_{1-x}Ge_6$ series of polar intermetallics (R = Rare-Earth Metal), Inorg. Chem. 54 (2015) 2411–2424, https://doi.org/10.1021/ic5030313.

[18] R. Freccero, P. Solokha, D.M. Proserpio, A. Saccone, S. De Negri, A new glance on R_2MGe_6 (R = rare earth metal, M = another metal) compounds. An experimental and theoretical study of R_2PdGe_6 germanides, Dalt. Trans. 46 (2017) 14021–14033, https://doi.org/10.1039/C7DT02686B.

[19] R. Freccero, P. Solokha, S. de Negri, A. Saccone, Y. Grin, F.R. Wagner, Polar-covalent bonding beyond the Zintl picture in intermetallic rare-earth germanides, Chem. - A Eur. J. (2019), https://doi.org/10.1002/chem.201900510.

[20] R. Freccero, L.C.J. Pereira, P. Solokha, S. De Negri, Flux growth, crystal structure, and chemical bonding of Yb_2PdGe_3, an AlB_2 superstructure within the Rare-Earth series, Inorg. Chem. 62 (2023), https://doi.org/10.1021/acs.inorgchem.2c03303.

[21] P. Solokha, R. Freccero, S. De Negri, D.M. Proserpio, A. Saccone, The $R_2Pd_3Ge_5$ (R = La–Nd, Sm) germanides: synthesis, crystal structure and symmetry reduction, Struct. Chem. 27 (2016) 1693–1701, https://doi.org/10.1007/s11224-016-0812-z.

[22] R. Freccero, S.H. Choi, P. Solokha, S. De Negri, T. Takeuchi, S. Hirai, P. Mele, A. Saccone, Synthesis, crystal structure and physical properties of $Yb_2Pd_3Ge_5$, J. Alloy. Compd. 783 (2019) 601–607, https://doi.org/10.1016/J.JALLCOM.2018.12.306.

[23] R. Freccero, S. De Negri, G. Rogl, G. Binder, H. Michor, P.F. Rogl, A. Saccone, P. Solokha, $La_2Pd_3Ge_5$ and $Nd_2Pd_3Ge_5$ compounds: chemical bonding and physical properties, Inorg. Chem. 60 (2021) 3345–3354, https://doi.org/10.1021/acs.inorgchem.0c03744.

[24] R.F.W. Bader, Atoms in Molecules: A Quantum Theory, Oxford University Press, Oxford, UK, 1990.

[25] Bruker, APEX4 v2022.10-0, (2022).

[26] Bruker, SAINT v8.30A, (2012).

[27] Bruker, XPREP v2014/2, (2014).

[28] Bruker, SADABS v2016/2, (2016).

[29] G.M. Sheldrick, SHELXL-2019/1, (2019).

[30] J. Rodriguez-Carvajal, FullProf, IUCr Newsl. (2001) 12–19.

[31] D. Schwarzenbach, LATCON: refine lattice parameters, (1996).

[32] CrystalMaker - Interactive Crystal & Molecular Modelling, (n.d.).

[33] Setaram, Calisto Software v1.38, (n.d.).

[34] A.T. Dinsdale, SGTE data for pure elements, Calphad 15 (1991) 317–425, https://doi.org/10.1016/0364-5916(91)90030-N.

[35] G. Krier, O. Jepsen, A. Burkhardt, O.K. Andersen, TB-LMTO-ASA Program (2000).

[36] U. Von Barth, L. Hedin, A local exchange-correlation potential for the spin polarized case. I, J. Phys. C. Solid State Phys. 5 (1972) 1629–1642, https://doi.org/10.1088/0022-3719/5/13/012.

[37] R. Dronskowski, P.E. Bloechl, Crystal orbital Hamilton populations (COHP): energy-resolved visualization of chemical bonding in solids based on density-functional calculations, J. Phys. Chem. 97 (1993) 8617–8624, https://doi.org/10.1021/j100135a014.

[38] B. Eck, wxDragon version 2.2.2-Basic, available at http://www.cohp.de/.

[39] V. Blum, R. Gehrke, F. Hanke, P. Havu, V. Havu, X. Ren, K. Reuter, M. Scheffler, Ab initio molecular simulations with numeric atom-centered orbitals, Comput. Phys. Commun. 180 (2009) 2175–2196, https://doi.org/10.1016/j.cpc.2009.06.022.

[40] F. Knuth, C. Carbogno, V. Atalla, V. Blum, M. Scheffler, All-electron formalism for total energy strain derivatives and stress tensor components for numeric atom-centered orbitals, Comput. Phys. Commun. 190 (2015) 33–50, https://doi.org/10.1016/j.cpc.2015.01.003.

[41] J.P. Perdew, A. Zunger, Self-interaction correction to density-functional approximations for many-electron systems, Phys. Rev. B 23 (1981) 5048–5079, https://doi.org/10.1103/PhysRevB.23.5048.

[42] A. Ormeci, H. Rosner, F.R. Wagner, M. Kohout, Y. Grin, Electron localization function in full-potential representation for crystalline materials, J. Phys. Chem. A. 110 (2006) 1100–1105, https://doi.org/10.1021/jp054727r.

[43] K. Klaus, H. Eschrig, Full-potential nonorthogonal local-orbital minimum-basis band-structure scheme, Phys. Rev. B - Condens. Matter Mater. Phys. 59 (1999) 1743–1757, https://doi.org/10.1103/PhysRevB.59.1743.

[44] M. Kohout, *DGrid*, version 4.6, Germany, 2014.

[45] U. Ayachit, The ParaView Guide: A Parallel Visualization Application, 2015.

[46] A. Baranov, Visualization plugin for ParaView, 2015.

[47] W.J. Boettinger, U.R. Kattner, K.-W. Moon, J. Perepezko, (2006) NIST Recommended Practice Guide: DTA and Heat-Flux DSC Measurements of Alloy Melting and Freezing, Elsevier, Kidlington, https://tsapps.nist.gov/publication/get_pdf.cfm?pub_id=901091 (Accessed January 22, 2024).

[48] E. Zintl, J. Goubeau, W. Dullenkopf, Salzartige Verbindungen und intermetallische Phasen des Natriums in flüssigem Ammoniak, Z. F. üR. Phys. Chem. 154A (1931) 1–46, https://doi.org/10.1515/ZPCH-1931-15402.

[49] Q. Lin, G.J. Miller, Electron-poor polar intermetallics: complex structures, novel clusters, and intriguing bonding with pronounced electron delocalization, Acc. Chem. Res. 51 (2018) 49–58, https://doi.org/10.1021/acs.accounts.7b00488.

[50] S. Ponou, S. Lidin, Exo-bonded six-membered heterocycle in the crystal structures of $RE_7Co_2Ge_4$ (RE = La–Nd), Dalt. Trans. 45 (2016) 18522–18531, https://doi.org/10.1039/C6DT03302D.

[51] Q. Lin, K. Aguirre, S.M. Saunders, T.A. Hackett, Y. Liu, V. Taufour, D. Paudyal, S. Budko, P.C. Canfield, G.J. Miller, Polar intermetallics $Pr_5Co_2Ge_3$ and $Pr_7Co_2Ge_4$ with planar hydrocarbon-like metal clusters, Chem. - A Eur. J. 23 (2017) 10516–10521, https://doi.org/10.1002/CHEM.201702798.

[52] A.V. Mudring, J.D. Corbett, Unusual electronic and bonding properties of the zintl phase Ca_5Ge_3 and related compounds. a theoretical analysis, J. Am. Chem. Soc. 126 (2004) 5277–5281, https://doi.org/10.1021/ja030216b.

[53] R. Freccero, J.-M. Hübner, Y. Prots, W. Schnelle, M. Schmidt, F.R. Wagner, U. Schwarz, Y. Grin, Excess" electrons in LuGe, Angew. Chem. Int. Ed. 60 (2021) 6457–6461, https://doi.org/10.1002/ANIE.202014284.

[54] R. Freccero, P. Solokha, D. Proserpio, A. Saccone, S. De Negri, $Lu_5Pd_4Ge_8$ and $Lu_3Pd_4Ge_4$: two more germanides among polar intermetallics, Crystals 8 (2018) 205, https://doi.org/10.3390/cryst8050205.

[55] R. Freccero, Y. Grin, F.R. Wagner, Polarity-extended $8 - N^{\mathrm{eff}}$ rule for semiconducting main-group compounds with the TiNiSi-type of crystal structure, Dalt. Trans. 52 (2023) 8222–8236, https://doi.org/10.1039/D3DT00621B.

[56] M. Kohout, R. Gumeniuk, A. Leithe-Jasper, Chemical bonding in the intermetallic compounds LaBeGe and ThBeGe, Eur. J. Inorg. Chem. 29 (2022) e202200383, https://doi.org/10.1002/ejic.202200383.

[57] M. Pani, A. Provino, V. Smetana, V. Shtender, C. Bernini, A.V. Mudring, P. Manfrinetti, Four ternary silicides in the La–Ni–Si system: from polyanionic layers to frameworks, CrystEngComm 24 (2022) 8219–8228, https://doi.org/10.1039/D2CE01007K.

[58] I. Doverbratt, S. Ponou, Y. Zhang, S. Lidin, G.J. Miller, Linear metal chains in Ca_2M_2X (M = Pd, Pt; X = Al, Ge): origin of the pairwise distortion and its role in the structure stability, Chem. Mater. 27 (2015) 304–315, https://doi.org/10.1021/cm503985h.

[59] P. Solokha, R.A. Eremin, T. Leisegang, D.M. Proserpio, T. Akhmetshina, A. Gurskaya, A. Saccone, S. De Negri, New quasicrystal approximant in the Sc–Pd system: from topological data mining to the bench, Chem. Mater. 32 (2020) 1064–1079, https://doi.org/10.1021/ACS.CHEMMATER.9B03767.

[60] O. Sichevych, Y. Prots, W. Schnelle, F.R. Wagner, Y. Grin, Polycation–polyanion architecture of the intermetallic compound $Mg_{3-x}Ga_{1+x}Ir$, 2022, Vol. 27, Page 659, Mol 27 (2022) 659, https://doi.org/10.3390/MOLECULES27030659.

[61] R. Freccero, S. De Negri, A. Saccone, P. Solokha, Solid state interactions in the La-Au-Mg system: phase equilibria, novel compounds and chemical bonding, Dalt. Trans. 49 (2020) 12056, https://doi.org/10.1039/d0dt02359k.

[62] R. Freccero, P. Solokha, S. De Negri, Unpredicted but it exists: trigonal Sc_2Ru with a significant metal-metal charge transfer, Inorg. Chem. 60 (2021) 10084–10088, https://doi.org/10.1021/acs.inorgchem.1c01168.

[63] L. Agnarelli, Y. Prots, R. Ramlau, M. Schmidt, U. Burkhardt, A. Leithe-Jasper, Y. Grin, $Mg_{29-x}Pt_{4+y}$: chemical bonding inhomogeneity and structural complexity, Inorg. Chem. 61 (40) (2022) 14148–16155, https://doi.org/10.1021/acs.inorgchem.2c02653.

[64] L. Agnarelli, Y. Prots, M. Schmidt, M. Krnel, E. Svanidze, U. Burkhardt, A. Leithe-Jasper, Y. Grin, Be_3Ru: polar multiatomic bonding in the closest packing of atoms, ChemistryOpen 11 (2022) e202200118, https://doi.org/10.1002/OPEN.202200118.

[65] L. Agnarelli, A. Ormeci, Y. Prots, M. Krnel, E. Svanidze, M. Schmidt, U. Burkhardt, Y. Grin, A. Leithe-Jasper, Stability of the atomic arrangement in Laves phases $Be_2Fe_{1-x}Os_x$ ($0 \le x \le 0.75$) and $Be_2Fe_{1-x}Ru_x$ ($x \approx 0.5$), J. Alloy. Compd. 968 (2023) 171911, https://doi.org/10.1016/J.JALLCOM.2023.171911.

[66] L. Salamakha, O. Sologub, B. Stöger, H. Michor, E. Bauer, P. Rogl, S. Mudry, Electronic and structural properties of $Y_6Pt_{13}X_4$, site occupancy variants of the $Ba_6Na_{16}N$ subnitride (X = Al, Ga), Dalt. Trans. 52 (2023) 6085–6096, https://doi.org/10.1039/D3DT00292F.

[67] A. Martinelli, D. Ryan, J. Sereni, C. Ritter, A. Leineweber, I. Čurlík, R. Freccero, M. Giovannini, Magnetic phase separation in the $EuPdSn_2$ ground state, J. Mater. Chem. C 11 (2023) 7641–7653, https://doi.org/10.1039/D3TC00764B.

[68] A. Amon, E. Svanidze, A. Ormeci, M. König, D. Kasinathan, D. Takegami, Y. Prots, Y. Liao, K. Tsuei, L.H. Tjeng, A. Leithe-Jasper, Y. Grin, Interplay of atomic interactions in the intermetallic semiconductor Be_5Pt, Angew. Chem. Int. Ed. 58 (2019) 15928–15933, https://doi.org/10.1002/anie.201909782.

[69] M. Armbrüster, Intermetallic compounds in catalysis – a versatile class of materials meets interesting challenges 21 (2020) 303–322, https://doi.org/10.1080/14686996.2020.1758544.

[70] I. Antonyshyn, A.M. Barrios Jiménez, O. Sichevych, U. Burkhardt, I. Veremchuk, M. Schmidt, A. Ormeci, I. Spanos, A. Tarasov, D. Teschner, G. Algara-Siller, R. Schlögl, Y. Grin, Al_2Pt for oxygen evolution in water splitting: a strategy for creating multifunctionality in electrocatalysis, Angew. Chem. Int. Ed. 59 (2020) 16770–16776, https://doi.org/10.1002/ANIE.202005445.

[71] R. Freccero, E. Spennati, G. Garbarino, P. Riani, Intermetallic based materials for Sabatier reaction: surface understanding, performance assessment and comparison with commercial catalyst, Appl. Catal. B Environ. 343 (2024) 123532, https://doi.org/10.1016/J.APCATB.2023.123532.

[72] A.M. Barrios Jiménez, A. Ormeci, U. Burkhardt, S.G. Altendorf, F. Kaiser, I. Veremchuk, G. Auffermann, Y. Grin, I. Antonyshyn, Intermetallic compounds M_2Pt (M = Al, Ga, In, Sn) in the oxygen evolution reaction, Sustain. Energy Fuels. 5 (2021) 5762–5772, https://doi.org/10.1039/D1SE01190A.

[73] R. Freccero, E. Frick, C. Wilthorn, J.M. Hübner, New insights into the crystal chemistry of FeB-type compounds: the case of CeGe, Materials 15 (2022) 9089, https://doi.org/10.3390/ma15249089.

[74] F. Stegemann, C. Benndorf, R.St Touzani, B.P.T. Fokwa, O. Janka, Experimental and theoretical investigations of the polar intermetallics $SrPt_3Al_2$ and Sr_2Pd_2Al, J. Solid State Chem. 242 (2016) 143–150, https://doi.org/10.1016/J.JSSC.2016.07.019.

[75] M. Giovannini, I. Čurlík, R. Freccero, P. Solokha, M. Reiffers, J. Sereni, Crystal structure and magnetism of noncentrosymmetric Eu_2Pd_2Sn, Inorg. Chem. 60 (2021) 8085–8092, https://doi.org/10.1021/acs.inorgchem.1c00678.

[76] L. Vegard, Die Konstitution der Mischkristalle und die Raumfüllung der Atome, Z. F. üR. Phys. 5 (1921) 17–26, https://doi.org/10.1007/BF01349680.

[77] W. Biltz, Raumchemie der festen Stoffe, Verlag von Leopol Voss, Leipzig, 1934.

[78] E.-A. Zen, Validity of "Vegard's law" Amer. Min. 41 (1956) 523-524.

[79] R. Ferro, A. Saccone, Intermetallic chemistry, Pergamon Materials Series, 13, Elsevier, Kidlington, Oxford OX5, UK, 2008.

[80] W.B. Pearson, The Crystal Chemistry and Physics of Metals and Alloys, Wiley, New York, 1972.

[81] W. Bronger, R. Kniep, M. Kohout, Volume chemistry of nitrogen in binary metal nitrides and subnitrides, Z. F. üR. Anorg. Und Allg. Chem. 630 (2004) 117–121, https://doi.org/10.1002/ZAAC.200300311.

[82] W. Bronger, A. Baranov, F.R. Wagner, R. Kniep, Atomvolumina und Ladungsverteilungen in Nitridometallaten, Z. F. üR. Anorg. Und Allg. Chem. 633 (2007) 2553–2557, https://doi.org/10.1002/ZAAC.200700413.

[83] A. Baranov, M. Kohout, F.R. Wagner, Y. Grin, R. Kniep, W. Bronger, On the volume chemistry of solid compounds: the legacy of Wilhelm Biltz, Z. F. üR. Anorg. Und Allg. Chem. 634 (2008) 2747–2753, https://doi.org/10.1002/ZAAC.200800331.

[84] W. Bronger, R. Kniep, M. Kohout, Zur Raumchemie des Wasserstoffs in binären und ternären Metallhydriden, (2005). doi:10.1002/zaac.200400382.

[85] A. Baranov, M. Kohout, F.R. Wagner, Y. Grin, W. Bronger, Spatial chemistry of the aluminium-platinum compounds: a quantum chemical approach, Z. Fur Krist. 222 (2007) 527–531, https://doi.org/10.1524/zkri.2007.222.10.527.

[86] Y. Grin, A. Fedorchuk, R.J. Faria, F.R. Wagner, Atomic charges and chemical bonding in Y-Ga compounds, Crystals 8 (2018), https://doi.org/10.3390/cryst8020099.

[87] L. Agnarelli, Y. Prots, M. Krnel, E. Svanidze, M. König, M. Schmidt, U. Burkhardt, A. Leithe-Jasper, Y. Grin, Charge transfer in Be−Ru compounds, Chem. - A Eur. J. (2023), https://doi.org/10.1002/CHEM.202302301.

[88] A. Slobodskyy, T. Slobodskyy, T. Ulyanenkova, S. Doyle, M. Powalla, T. Baumbach, U. Lemmer, In-depth analysis of the $CuIn_{1-x}Ga_xSe_2$ film for solar cells, structural and optical characterization, Appl. Phys. Lett. 97 (2010) 251911, https://doi.org/10.1063/1.3529939.

[89] A. Goetzberger, C. Hebling, H.W. Schock, Photovoltaic materials, history, status and outlook, Mater. Sci. Eng. R. Rep. 40 (2003) 1–46, https://doi.org/10.1016/S0927-796X(02)00092-X.

[90] F. Simon, N. Couvrat, C. Bilot, S. Marinel, S. Malo, G. Coquerel, The solid solution between $NaClO_3$ and $NaBrO_3$ revisited, Minerals 13 (2023) 1006, https://doi.org/10.3390/min13081006.

[91] H.-R. Wenk, A. Bulakh, Solid solutions. In: Minerals: Their Constitution and Origin. Cambridge, Cambridge University Press, 2004, pp. 305–310, https://doi.org/10.1017/CBO9780511811296.020.

[92] I.V. Pekov, N.V. Zubkova, I.O. Galuskina, J. Kusz, N.N. Koshlyakova, E.V. Galuskin, D.I. Belakovskiy, M.O. Bulakh, M.F. Vigasina, N.V. Chukanov, S.N. Britvin, E. G. Sidorov, Y. Vapnik, D.Y. Pushcharovsky, Calciolangbeinite-*O*, a natural orthorhombic modification of $K_2Ca_2(SO_4)_3$, and the langbeinite–calciolangbeinite solid-solution system, Mineral. Mag. 86 (2022) 557–569, https://doi.org/10.1180/MGM.2021.95.